Structure of the human cation–chloride cotransport KCC1 in an outward-open state

Yongxiang Zhao[a] , Jiemin Shen[b] , Qinzhe Wang[a], Manuel Jose Ruiz Munevar[c] , Pietro Vidossich[c], Marco De Vivo[c] , Ming Zhou[b], and Erhu Cao[a,1]

Cation–chloride cotransporters (CCCs) catalyze electroneutral symport of Cl^- with Na^+ and/or K^+ across membranes. CCCs are fundamental in cell volume homeostasis, transepithelia ion movement, maintenance of intracellular Cl^- concentration, and neuronal excitability. Here, we present a cryoelectron microscopy structure of human K^+–Cl^- cotransporter (KCC)1 bound with the VU0463271 inhibitor in an outward-open state. In contrast to many other amino acid–polyamine–organocation transporter cousins, our first outward-open CCC structure reveals that opening the KCC1 extracellular ion permeation path does not involve hinge-bending motions of the transmembrane (TM) 1 and TM6 half-helices. Instead, rocking of TM3 and TM8, together with displacements of TM4, TM9, and a conserved intracellular loop 1 helix, underlie alternate opening and closing of extracellular and cytoplasmic vestibules. We show that KCC1 intriguingly exists in one of two distinct dimeric states via different intersubunit interfaces. Our studies provide a blueprint for understanding the mechanisms of CCCs and their inhibition by small molecule compounds.

biochemistry | structural biology | ion transport

Secondary active cation–chloride cotransporters (CCCs) harness the Na^+ and/or K^+ gradients that exist across all animal cells to move Cl^- into or out of cells in an electroneutral fashion (1, 2). CCCs play fundamental roles in a multitude of biological processes such as transepithelial ion movements, cell volume homeostasis, and regulation of intracellular Cl^- concentration ($[Cl^-]_i$) and neuronal excitability (3–6). For example, in response to hypotonic challenge, K^+–Cl^- cotransporters (KCCs) extrude Cl^- and K^+ to defend against cell swelling via concomitant obligatory water efflux (7, 8). In most mature neurons, KCC2 functions as a major Cl^- extruder to maintain $[Cl^-]_i$ below electrochemical equilibrium such that inhibitory neurotransmitters (e.g., γ-aminobutyric acid [GABA]) stimulate Cl^- influx via pentameric ligand-gated Cl^- channels and lead to hyperpolarization (9). Thus, mutations in KCC2 (or KCC3) cause a variety of neurological diseases such as epilepsy, autism, and schizophrenia (10–17). KCCs are therefore emerging attractive therapeutic targets in the nervous system as well as in nonexcitable cells. KCC activators were indeed used to restore inhibitory GABAergic neurotransmission in various brain disorders and psychiatric conditions (9, 18–22). Conversely, inhibiting KCC activity in red blood cells has been shown to counteract characteristic sickle cell dehydration, thereby providing a promising therapeutic strategy to treat sickle cell anemia (23, 24). Finally, NKCC2 and NCC, two CCC members in the kidney, are inhibited by loop and thiazide diuretics used to treat hypertension and edema (25, 26), albeit with undesirable side effects such as hearing loss (27, 28).

Despite these key physiological functions and disease implications, how CCCs transport ions across membranes and how therapeutically useful small molecules inhibit this process remain largely undefined in structural terms. Previous structures of CCCs have revealed these proteins' dimeric architecture, overall domain organization, and ion binding mechanisms (29–36). These structures demonstrate that the CCC transport core consists of two inverted repeats of five-helix bundles (i.e., transmembrane (TM)1–TM5 and TM6–TM10). The TM1 and TM6 helices lie at the center of the ion transport path and break α-helical geometry roughly at the middle of the lipid bilayer where ion binding sites are organized around these discontinuous hinge regions. The remaining TM11 and TM12 helices and cytoplasmic C-terminal and extracellular domains contribute to dimeric assembly. Unfortunately, existing CCC structures have captured only the inward-open state, which represents just one of several conformations along each transport cycle. Structures of other amino acid–polyamine–organocation (APC) transporter superfamily members have been solved in multiple states (37, 38), but are challenging to extrapolate to CCCs due to low sequence homology and

Significance

Cation–chloride cotransporters (CCCs) shuttle Na^+, K^+, and Cl^- across membranes. However, it remains unclear how CCCs alternate between transport states so they can load ions from one side of a membrane for release into the other side. Moreover, CCCs are targeted by compounds that are used as clinical medicines for treating hypertension/edema or as pharmacological tools for dissecting CCC functions. How these pharmacological agents interact with CCCs is yet to be elucidated. Our structure of K^+–Cl^- cotransporter (KCC) 1 bound with the VU0463271 inhibitor highlights the extracellular ion translocation pathway as a promising site for developing CCC modulators and defines conformational changes critical for ion transport in KCC1, which are distinct from those observed in related transporter cousins.

divergent biophysical properties. For these reasons, a structural understanding of CCC transport cycle remains elusive. Finally, structures of CCCs bound to small molecule modulators would help to reveal their sites and mechanisms of action and facilitate medicinal chemistry and computational docking efforts to further improve specificity and potency of these drugs.

Here we report two cryoelectron microscopy (cryo-EM) structures that represent human KCC1 trapped in an inward-open state or arrested in its elusive outward-open state by the KCCs inhibitor VU0463271 (39, 40). We show that each KCC1 transport cycle entails rocking of TM3 and TM8 helices coupled with displacements of TM4, TM9, and a highly conserved short helix within the first intracellular loop (ICL1), leading to alternate opening and closing of extracellular and cytoplasmic ion permeation paths. VU0463271 inhibits KCC1 by wedging into the extracellular ion transport path, breaking ionic gating interactions at the extracellular entryway and leading to opening of an extracellular vestibule. KCC1 can adopt two distinct dimeric architectures via association of domains that may be subjected to regulation by phosphorylation and cellular factors. Our structures reveal conformational changes along the CCC reaction pathway and may facilitate rational development of KCCs modulators for the treatment of various brain disorders.

Results

The VU0463271 Inhibitor Traps KCC1 in an Outward-Open State.
To structurally characterize the CCC transport cycle beyond the existing inward-open state (29–36), we utilized the VU0463271 inhibitor to trap KCC1 in an outward-open conformation. VU0463271 and related compounds compete with K^+ for the same or overlapping binding site along the ion transport pathway of KCCs (40). However, because it is much larger than a permeating K^+ ion, we reasoned that it could physically hold open the extracellular entryway. Using the above strategy, we solved two structures of the full-length human KCC1 both assembled as a dimer by single-particle cryo-EM: one in 150 mM KCl at 3.25-Å resolution in which the two interdigitating C-terminal domains sit beneath the transmembrane core of a neighboring subunit and another in 150 mM NaCl bound with VU0463271 at 3.49-Å resolution in which the C-terminal domains are not resolved, possibly because they assume a range of orientations with respect to the transmembrane domains (Fig. 1A and *SI Appendix*, Figs. S1–S7).

KCC1 assumes an inward-open conformation in 150 mM KCl as do reported CCC structures. In contrast, VU0463271 selectively binds to and stabilizes a new conformation where a large extracellular vestibule would allow for unobstructed access of K^+ and Cl^- ions to the central ion binding sites (Fig. 1B). Because the intracellular exit is occluded, the VU0463271-bound map represents KCC1 in an outward-open state, the first of its kind within the CCC family. Comparison of our two KCC1 structures showed that opening of the extracellular entryway mainly involves displacements of TM3 and TM9, as well as subtle movement of TM10 away from the central ion translocation path; the intracellular vestibule is closed by opposite movements of TM8 and TM4 (Fig. 1C and *SI Appendix*, Fig. S8A). TM4 and TM9 also move downward toward the inner membrane. VU0463271 likely facilitates these rigid body movements of helices by directly engaging TM3 and TM10, pushing these two helices away from the center of the extracellular vestibule and ultimately displacing the three remaining adjacent helices. Consistent with our structural findings, crosslinking and solvent accessibility studies indicate that TM10 of
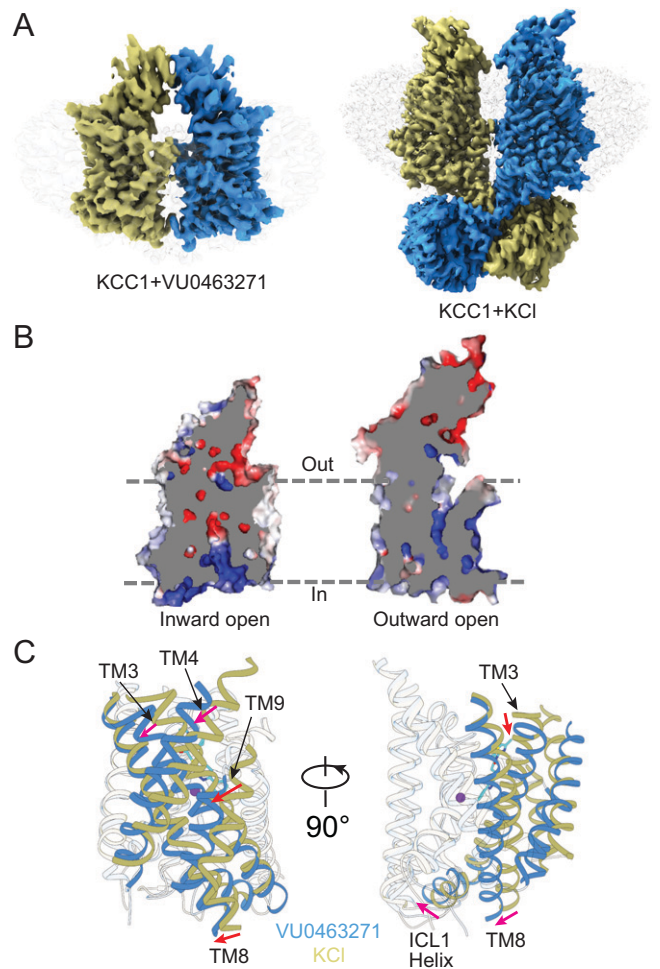

Fig. 1. The VU0463271 inhibitor arrests KCC1 in an outward-open state. (*A*) Side view of KCC1 bound with the VU0463271 inhibitor. Individual subunits are color coded. Densities of detergent micelle (gray) are rendered semitransparent. (*B*) "Slab" views of the inward-open (KCl) and outward-open (VU0463271 bound) KCC1, highlighting an extracellular vestibule in the VU0463271-bound KCC1 structure if the inhibitor is removed and an intracellular exit in the inhibitor-free KCC1 structure. (*C*) Superimposition of KCC1 structures in VU0463271-bound or inhibitor-free (150 mM KCl) states. K^+ ion and the inhibitor are shown as a purple sphere and sticks, respectively. Movements of TM3, TM8, TM 4, TM9, and the ICL1 helix are highlighted with red arrows. See also *SI Appendix*, Figs. S1–S8.

Na^+–K^+–2 Cl^- (NKCC1) undergoes movements during ion transport (41).

The VU0463271 Binding Site in KCC1.
VU0463271 stabilizes an outward-open KCC1 conformation by fitting into an extracellular pocket formed by TM helices 1b, 6a, 3, and 10. VU0463271 binding not only plugs the extracellular entryway, but may also sterically hinder KCC1 from isomerizing into other states (Fig. 1C). VU0463271 establishes a multitude of polar and hydrophobic contacts with residues along the extracellular ion transport pathway. At the mouth of the extracellular entryway, the VU0463271 4-methyl-2-thiazolyl group wedges between Arg140 and Glu222 (Fig. 2 A and B), breaking the salt bridge that closes the extracellular gate as seen in the inward-open structure (Fig. 2C). Here, the 4-methyl-2-thiazolyl group interacts with residues Glu222, Ile223, and Tyr227 on TM3, as well as residues on TM1b (e.g., Val135) via hydrogen bonding and hydrophobic packing interactions. The 4-methyl group establishes hydrophobic interactions with Ile223, rationalizing previous observations that removal of this group
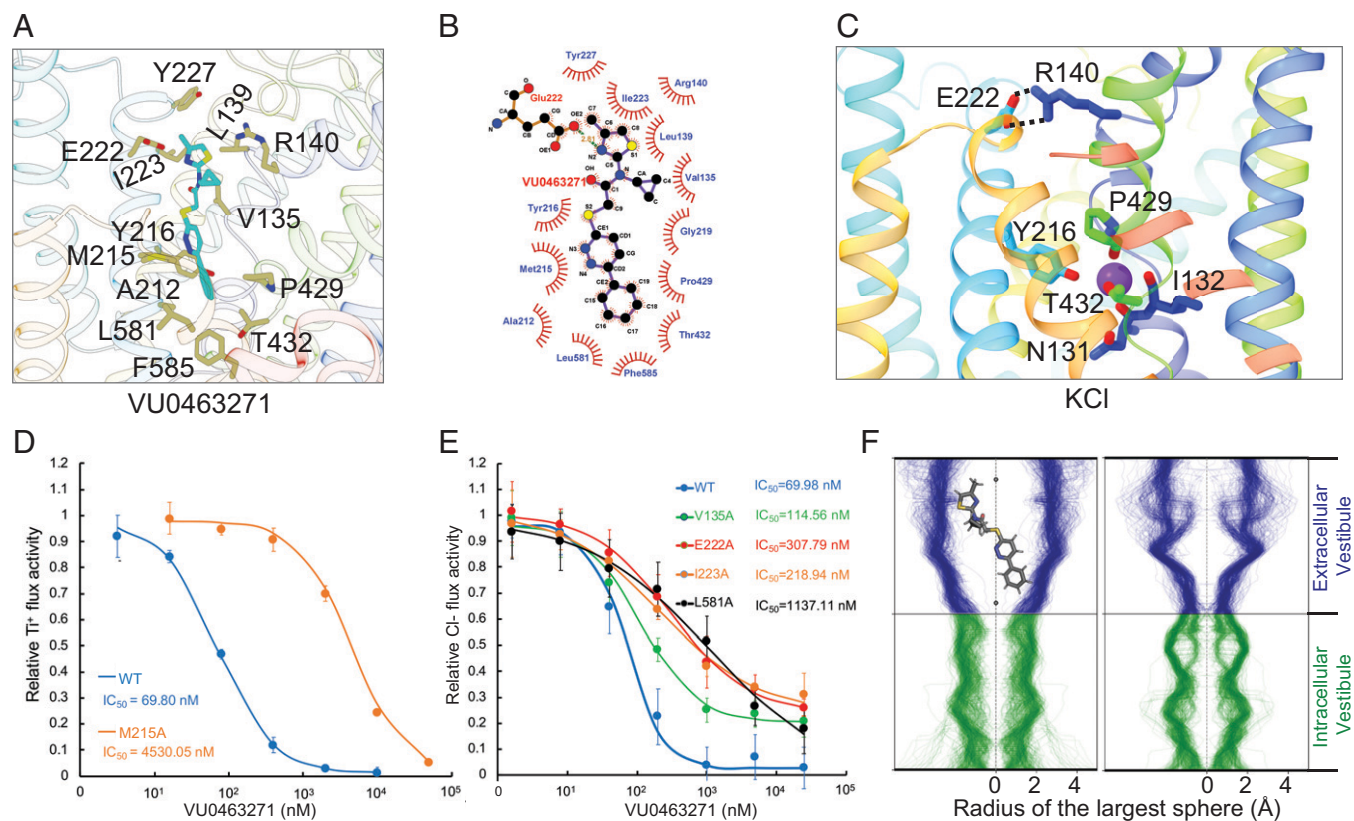
Fig. 2. The VU0463271 binding site in KCC1. (*A*) VU0463271 breaks the extracellular ionic gate formed between E222 and R140 and interacts with residues along the extracellular ion permeation pathway of KCC1. (*B*) A 2D representation of VU0463271 interactions with residues along the KCC1 extracellular ion permeation path. Each eyelash indicates a hydrophobic interaction. (*C*) The extracellular gate and K$^+$ binding site are intact in the KCC1 structure in the inhibitor-free state (150 mM KCl). (*D*) The wild-type KCC1 is inhibited by VU0463271 with an IC$_{50}$ of 69.8 nM, whereas the M215A mutant exhibits reduced sensitivity to the inhibitor with an IC$_{50}$ of 4.53 μM in liposomes (*n* = 3). (*E*) Four VU0463271 binding site mutants show reduced sensitivity to the inhibitor in insect cells (*n* = 6). (*F*) Molecular dynamics simulation validation of the binding pose of VU0463271. Note that the inhibitor retains its experimentally observed binding pose and the extracellular vestibule remains open over a 450-ns simulation (*Left*), whereas the extracellular ion permeation path narrows when the inhibitor is removed (*Right*). See also *SI Appendix*, Figs. S9 and S10, as well as Movie S1.

diminishes potency of related inhibitors (40). An analogous salt bridge exists at the extracellular gate of NKCC1 (30, 31, 34), suggesting that opening of the extracellular entryway may also entail salt bridge disruption in other CCCs as well. Deeper toward the central ion binding site, the phenyl-3-pyridazinyl group engages with a number of residues located on TM6a, TM3, and TM10, including Tyr216 that would otherwise participate in coordination of a permeating K$^+$ ion (Fig. 2 *A–C* and *SI Appendix*, Fig. S9 *A* and *B*). The fact that VU0463271 and K$^+$ share coordinating residues explains why potency of related compounds decreases as extracellular K$^+$ concentrations increase (40). M215 also participates in binding VU0463271, hinting at a common ligand binding site within the CCC family as the equivalent M382 residue in NKCC1 is also essential for inhibition by bumetanide (42).

The exact binding pose of VU0463271 requires an atomic resolution structure; we thus validated the VU0463271 binding site observed in our structure in two ways. First, we reconstituted the wild-type KCC1 and M215A mutant into liposomes and measured their VU0463271 sensitivity using a thallium (a congener of K$^+$) ion flux assay. M215A exhibited an ~65-fold loss of sensitivity to VU0463271 (half maximal inhibitory concentration [IC$_{50}$] = 4.53 μM, compared to 69.8 nM for wild-type KCC1 as shown in Fig. 2*D* and *SI Appendix*, Fig. S10 *H* and *I*). We established a Cl$^-$ efflux assay for KCC extruders in insect cells (*SI Appendix*, Fig. S10 *A* and *B*). Using this assay, we similarly showed that four additional VU0463271 binding site

mutants (V135A, E222A, I223A, and L581A) exhibit reduced sensitivity to the inhibitor in insect cells (Fig. 2*E* and *SI Appendix*, Fig. S10 *C–G*). Second, we validated the pose of VU0463271 seen in our structure using molecular dynamic (MD) simulations. We showed that VU0463271 remains within the experimentally observed binding pocket throughout the 450-ns MD simulations (*SI Appendix*, Fig. S9 *C* and *D*). Consequently, the volume of the extracellular/intracellular vestibules remained unaltered (Fig. 2*F*). However, when the inhibitor is removed and replaced with H$_2$O and K$^+$/Cl$^-$ ions during simulation, the extracellular vestibule shrinks and the intracellular vestibule remains closed (Fig. 2*F*). Taken together, our VU0463271-bound KCC1 structure highlights the extracellular ion permeation path as a critical site for inhibition of KCC1, and possibly other CCCs as well (Movie S1).

Ion Translocation Pathway of KCC1. Previous structure–function studies of CCCs have largely focused on their ion coordinating residues (29–36). Our outward-open KCC1 structure now defines an extracellular ion translocation pathway leading to the central ion binding sites, allowing us to interrogate the roles of residues that line the extracellular vestibule via site-directed mutagenesis (Fig. 3*A*). We found that mutations of residues, which located either at the extracellular mouth (L139A, I223A, L574A, D575A, E222A, and R140Q) or deeper toward the central ion binding sites (V135A, I136A, and M215A), all significantly reduced transport activity of KCC1 (Fig. 3*B* and *SI Appendix*, Fig. S11).
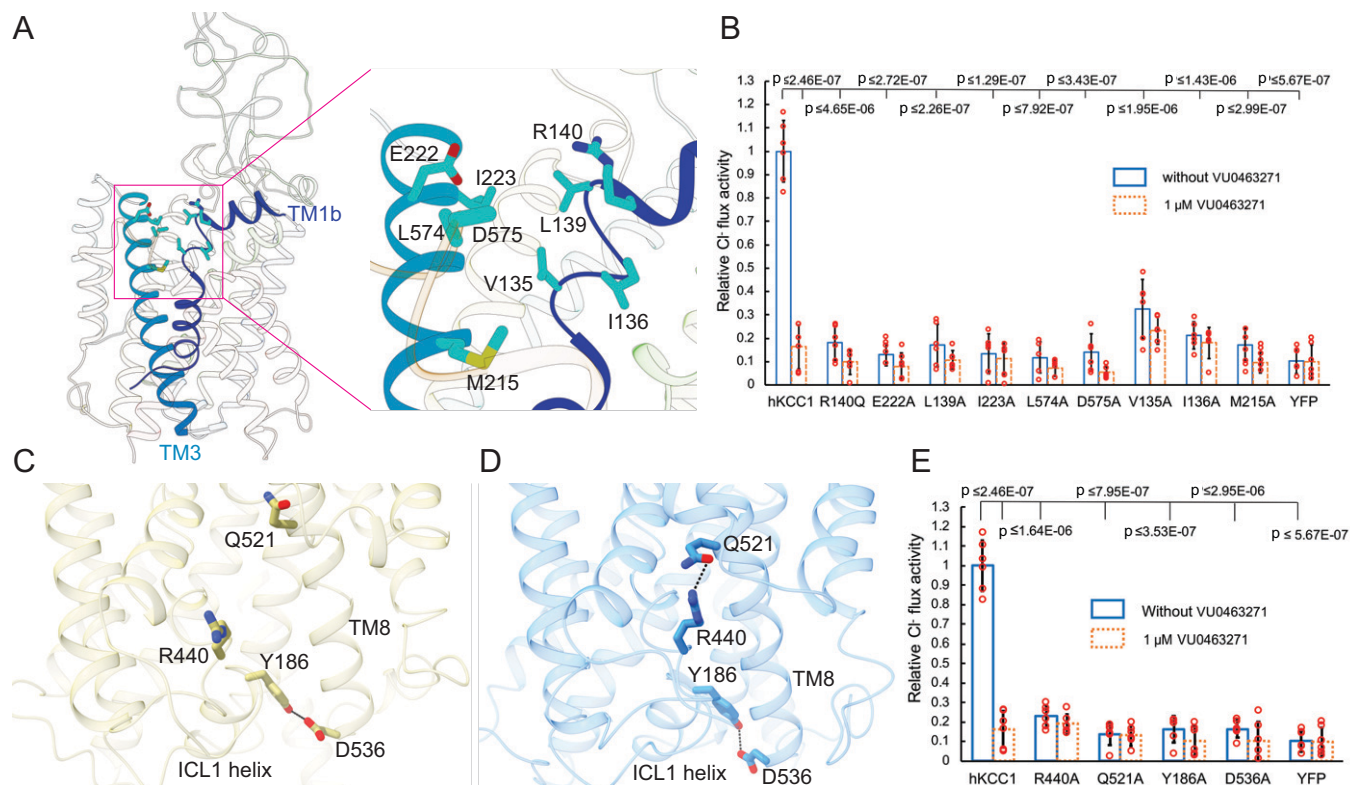
Fig. 3. The ion translocation pathway in KCC1. (*A*) The outward-open KCC1 structure highlights several residues that line the extracellular vestibule. (*B*) Cl⁻ transport rates of wild type and mutants designed to perturb KCC1 extracellular vestibule in Sf9 cells. Each circle represents one kinetic measurement of a single sample in a 96-well plate. Student's *t* tests were used for statistical analyses (*n* = 6). (*C*) In the inhibitor-free state (150 mM KCl), the intracellular gate is broken as R440 on TM6b is ~10 Å away from Q521 on TM8. (*D*) In the VU0463271-bound KCC1 structure, R440 establishes gating interactions with Q521 due to an inward movement of TM8. In both structures, the ICL1 helix is coupled to TM8 via hydrogen bonding interactions between Y186 and D536. (*E*) Cl⁻ transport rates of wild-type KCC1 and intracellular gate mutants in Sf9 cells. Each circle represents one kinetic measurement of a single sample in a 96-well plate. Student's *t* tests were used for statistical analyses (*n* = 6). See also *SI Appendix*, Figs. S11 and S12.

Based on the alternating access model, opening of an extracellular vestibule in KCC1 must be tightly coupled to closure of the cytoplasmic exit. By comparing our outward- and inward-open KCC1 structures, we determined that the cytoplasmic exit is occluded via a concerted movement of TM8, the TM6b–TM7 intracellular loop 3 (ICL3), and the short helix within ICL1 toward the central ion translocation path (Fig. 1*C*). The most pronounced movements occur in TM8 and the ICL1 helix during KCC1 isomerization. In VU0463271-bound KCC1, the ICL1 helix lies almost parallel to the inner leaflet of the bilayer, intercalating among the cytoplasmic ends of TM helices 2, 3, 6b, 8, and 10 to plug the intracellular vestibule. In particular, hydrogen bonding interactions between Tyr186 and Asp536 couple the short ICL1 helix directly to TM8, triggering a displacement of both helices to close the intracellular exit (Fig. 3 *C* and *D*). Of note, ICL1 is a highly conserved signature motif among CCCs, and missense mutations within this region inactivate NKCC transporters, instigating salt-wasting hypotensive Bartter syndrome in humans (43, 44).

These movements foster the establishment of new gating interactions that may contribute to closure of the cytoplasmic exit. In the VU0463271-bound KCC1 structure, Arg440 at the cytoplasmic end of TM6b, hydrogen bonds with Gln521 in TM8 (Fig. 3*D*); in the inward-open state, Arg440 is separated from Gln521 by up to 10 Å measured as distance between mainchain atoms (Fig. 3*C*). We showed that mutations of these two residues, as well as the Tyr186/Asp536 pair that couples the TM8 and ICL1 helices, all reduce KCC1 transporter activity (Fig. 3*E* and *SI Appendix*, Fig. S12*A*). We further showed that mutations of equivalent residues in KCC3 (R505A and

Q586A) also abolish ion transport activity (*SI Appendix*, Fig. S12 *B* and *C*), confirming a conserved gating role for these two residues in KCCs. Of note, although these two residues are strictly conserved in all KCC isoforms and thus are likely crucial for isomerization of these transporters among distinct transport states, they are replaced by hydrophobic residues in NKCC1 (*SI Appendix*, Fig. S13). This observation suggests that Na⁺-dependent CCCs may use a different set of residues to close their intracellular exits.

Alternating access in KCC1 does not involve hinge-bending motion around the discontinuous regions of TM1 and TM6 as commonly observed in LeuT and neurotransmitter reuptake transporters (45, 46). Superimposition of our outward- and inward-open KCC1 structures showed that the TM1, TM2, TM6, and TM7 helix bundle, which is commonly referred to as the "core domain" in the LeuT fold (38), remains static with a rmsd of ~1.2 Å (*SI Appendix*, Fig. S8*A*). On the contrary, TM3 and TM8 helices within the so-called "scaffold domain" undergo rock motion, leading to reciprocal opening and closing of the extracellular and cytoplasmic ion permeation pathways. Mobility of the KCC1 bundle helices may be restricted by tight association between the TM2 and TM11 helices, including a KCC-specific disulfide bond (C163–C626) that covalently connects these two helices (*SI Appendix*, Fig. S8*B*). As a caveat, we noticed that the scaffold domain, when extracted from the outward- and inward-open structures, also superimposes, but structural comparison using the scaffold domain as a reference would imply that a KCC1 transport cycle entails movements of not only the core domain as seen in LeuT, but also TM11, TM12, and the large extracellular domains.

Human KCC1 Adopts Two Distinct Dimeric Architectures. In keeping with previously reported CCC structures (29–32, 34–36), KCC1 also assembles as a dimer in both conditions, albeit assuming drastically distinct overall architecture due to association via different intersubunit interfaces (Fig. 4 *A* and *B*). In the 150-mM KCl condition, the KCC1 dimer resembles structures of zebrafish NKCC1 and other KCCs where an inverted V-shaped helix-turn-helix structure formed by TM11 and TM12 helices constitutes the principal dimeric interface with a buried surface of 352.2 Å² within the lipid bilayer in addition to the interdigitating cytosolic C-terminal domains with a buried surface of 2,480.6 Å² (Fig. 4*B*). In particular, an α-helix (^{666}Arg–Glu^{682}), which immediately follows TM12, runs almost parallel to the inner membrane and establishes extensive hydrophobic interactions with the same helix oriented in an opposite direction from a second KCC1 subunit. In
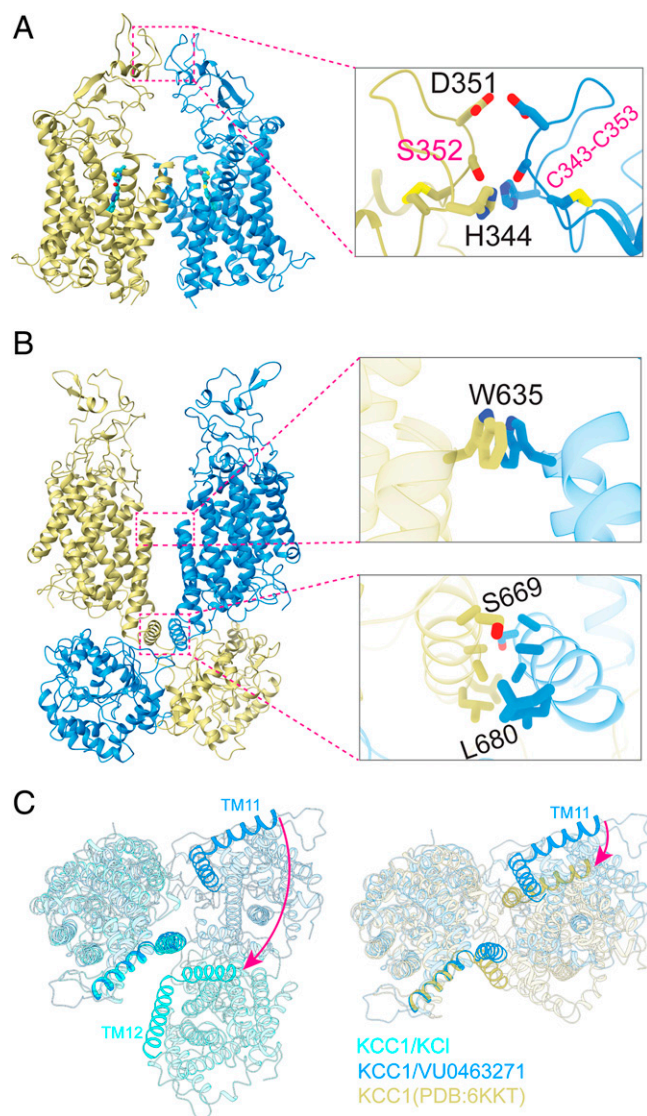
the VU0463271-bound KCC1 structure, however, cytosolic domains are not resolved in our map, consistent with reference free two-dimensional (2D) class averages that also only show a cloud of fuzzy densities for the cytosolic domains (*SI Appendix,* Fig. S1*C*). Cytosolic domains may not participate in dimer assembly in the VU0463271-bound KCC1 structure. The direct protein contacts within the lipid bilayer are also insignificant with a buried surface of 52.3 Å². Instead, an extracellular domain (ECD), formed by a stretch of ~120 residues between TM5 and TM6, participates in homotypic interactions with the same structure from a second KCC1 subunit with a buried surface of 125.7 Å² (Fig. 4*A*). In particular, residues (i.e., His344, Asp351, and Ser352) protrude from a finger-like loop, a structure that is possibly rigidified by a conserved disulfide bond found in all KCC isoforms, pointing their side chains toward the central twofold axis to establish polar contacts with the same set of residues from another subunit. We note that nonprotein densities, which possibly represent copurified endogenous lipids (or detergents), are found in the large void between the two subunits, suggesting that lipid-mediated association within the lipid bilayer may additionally stabilize the KCC1 dimer within the native membrane in addition to interactions among the ECD (*SI Appendix,* Fig. S7). Our VU0463271-bound KCC1 dimer resembles a previously reported KCC1 structure in which the C-terminal domain was also not resolved (32), although relative orientation of two subunits, and consequently, intersubunit interfaces are not identical in these two structures (Fig. 4*C*).

Discussion

One unexpected finding emerged from our structural studies is that KCC1 isomerizes from the outward-open to the inward-open state without evoking drastic flexing motions of TM1 and TM6 half-helices around the discontinuous hinge regions as commonly observed in LeuT and many other APC transporters (38, 45–48). Instead, morphing between inward- and outward-open KCC1 structures shows that outward movements of TM3 pivoted at its cytoplasmic end, together with a slight displacement of TM10, resulting in the opening of an extracellular pathway leading to the central ion binding sites (Fig. 5 and Movies S2 and S3). Such subtle conformational changes associated with ion transport by CCCs possibly explain why they can catalyze much higher rates of substrate movement across membrane than many other APC transporters as previously noted (42). Although such displacements of helices were facilitated by VU0463271 binding in our current structure, they may be similarly triggered by extracellular K⁺ and Cl⁻ in vivo as ions could conceivably break extracellular salt bridge gating interactions involving Glu222 on TM3. Moreover, Tyr589 on TM10 participates in Cl⁻ binding at the S_{Cl2} site (32, 35), so coordination (or dissociation) of Cl⁻ to this site could similarly contribute to movement of TM10. Conversely, inward movement of TM8 pivoted at the extracellular end, coupled with a concerted movement of the ICL1 helix, occludes the cytoplasmic exit. Such opposite motions of TM3 and TM8 during transition among distinct transport states appear to be directly coupled, as these two long tilted helices lie next to each other. In Na⁺-dependent CCCs, TM8 bears two Na⁺-coordinating residues, so it is conceivable that dynamic formation and rupture of the Na⁺ site may induce movements of TM8 during ion transport as seen in our KCC1 structures. Future studies of outward-open NKCC structures will help to resolve this possibility. Such structures could be determined de novo, but our outward-open KCC1 structure may also permit accurate
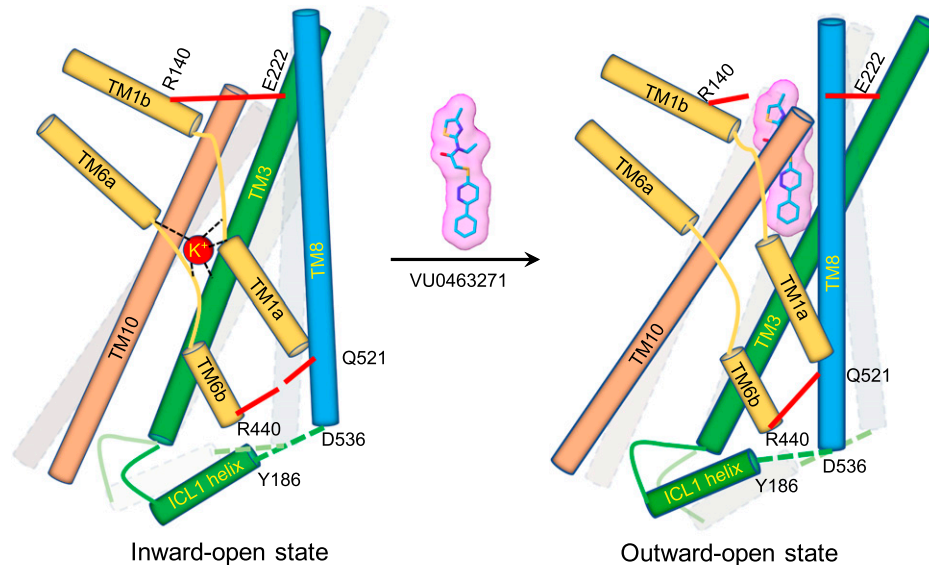

Fig. 4. KCC1 adopts a two-dimeric architecture. (*A*) Ribbon representation of the KCC1 dimer bound with VU0463271 is shown together with an enlarged view highlighting the dimer interface between the extracellular domains. (*B*) Ribbon representation of the KCC1 dimer in an inhibitor-free state (150 mM KCl) is shown together with enlarged views of two intersubunit interfaces. (*C*) Three human KCC1 structures, two of which are determined in this study, are aligned based on one subunit, highlighting distinct dimeric organizations as the second subunit is differently oriented with respect to the first superimposed subunit. TM11 and TM12 helices are shown in bright colors to illustrate rotation/displacement (red arrows) of the second subunits.

Fig. 5. Model of gating interactions and conformational changes in KCC1. In the inward-open state (inhibitor-free, 150 mM KCl), the intracellular gate is open as the gating interactions (R440–Q521) are broken, while the extracellular gate is closed by the salt bridge R140–E222. VU0463271 arrests KCC1 in an outward-open state by wedging into the extracellular ion permeation path. VU0463271 directly engages TM3 and TM10, breaks the extracellular gate, disrupts K⁺ coordination, and triggers a concerted movement of TM3, TM8, the ICL1 helix, and subtle movement of TM10 as well, fostering gating interactions (R440–Q521) that close the intracellular vestibule. See also Movies S2 and S3.

modeling of the comparable state in NKCCs based on the existing inward-open structures (30, 31, 34).

Another intriguing finding from our study is that KCC1 can adopt two drastically distinct dimeric architectures. The ECD represents the most divergent structure in primary sequence among four KCC isoforms (*SI Appendix*, Fig. S13), so it is unclear whether this domain can serve as a general dimerization module within all KCCs. Notwithstanding this important caveat, the remarkable plasticity in modes of dimeric assembly of KCC1 may suggest that conversion between these two dimeric forms could be intimately associated with activation of CCCs by (de)phosphorylation or by engagement of cellular factors such as creatine kinases (49–51).

NKCCs and NCC are the molecular targets of antihypertensive loop and thiazide diuretics (25, 26), and elucidating their sites and mechanisms of actions represents an important goal for further improving specificity and potency of these widely prescribed drugs via rational medicinal chemistry campaigns. Our VU0463271-bound KCC1 structure pinpoints the extracellular ion permeation path as an important molecular site for inhibition of CCCs. More broadly, in other APC transporters, the extracellular entryway is also frequently targeted by many competitive or allosteric inhibitors, including tryptophan and antidepressant citalopram that inhibit LeuT and serotonin transporter, respectively (52, 53). Diuretics may also trap NKCCs and NCC in outward-open conformations from the extracellular side as they are charged molecules and thus possibly cannot diffuse freely across the membrane barrier. Computational models of NKCC outward-open structures based on our outward-open KCC1 structure may provide useful models to study the modes of action of these loop diuretics, as well as to develop improved versions via computational drug docking campaigns.

Experimental Procedure

Expression and Purification of Human KCC1. The full-length human KCC1 isoform A gene (NG_033098.1) was amplified from human cDNA and cloned into a modified pFastBac1 vector downstream of the human cytomegalovirus (CMV) promotor. A maltose binding protein (MBP) followed by a tobacco etch virus (TEV) protease cleavage site was fused immediately before the N terminus of KCC1. This construct was expressed in HEK293S GnTI⁻/⁻ cells (American Type Culture Collection, CRL-3022) using the BacMam system as described (54). In brief, HEK293S GnTI⁻/⁻ cells, grown in suspension in Freestyle 293 expression medium (Invitrogen) at 37 °C in an orbital shaker, were transduced with human KCC1 baculoviruses when cell density reached ~2 × 10⁶/mL 8 to 12 h posttransduction; sodium butyrate was added to the culture to a final concentration of 5 mM to enhance protein expression; and temperature was reduced to 30 °C. Cells were harvested 72 h posttransduction and flash frozen in liquid nitrogen and stored at −80 °C until use. All protein purification steps were carried out at 4 °C unless stated otherwise. Membrane proteins were extracted for 1 h at room temperature in a buffer composed of (in millimoles) 50 Hepes (pH 7.4), 75 KCl, 75 NaCl, 0.5 Tris (2-carboxyethyl) phosphine (TCEP), 3 lauryl maltose neopentyl glycol (MNG-3), and 0.6 cholesteryl hemisuccinate Tris salt (CHS), 0.5 phenylmethylsulfonyl fluoride (PMSF), 5 μg/mL leupeptin, 1.4 μg/mL pepstatin A, 2 μg/mL aprotinin, and 10% glycerol. The supernatant was collected after centrifugation at 18,000 rpm for 30 min and then incubated with amylose resin (New England BioLabs) for 2 h. Human KCC1 protein was eluted from amylose resin with buffer composed of (in millimoles) 20 Hepes (pH 7.4), 150 KCl, 0.5 TCEP, 0.5 MNG-3, 0.1 CHS, and 20 maltose. The MBP fusion tag was removed by incubation with TEV protease overnight. Human KCC1 was further separated with a Superose 6 column using buffer composed of (in millimoles) 20 Hepes (pH 7.4), 150 KCl, 0.5 TCEP, 25 × 10⁻³ MNG-3, and 5 × 10⁻³ CHS; and peaks corresponding to human KCC1 were collected and concentrated for cryo-EM analyses. For preparing human KCC1 bound with VU0463271, human KCC1 was purified with a Superose 6 column using a K⁺ free buffer composed of (in millimoles) 20 Hepes (pH 7.4), 150 NaCl, 0.5 TCEP, 25 × 10⁻³ MNG-3, 5 × 10⁻³ CHS, and 25 × 10⁻³

VU0463271. The peaks corresponding to KCC1 were collected and supplemented with VU0463271 to a final concentration of 75 µM to incubate for 30 min at room temperature prior to cryo-EM analyses.

Proteoliposome Preparation and Tl$^+$ Flux Assay. The 1-palmitoyl-2-oleoyl-sn-glycero-3-phosphoethanolamine (POPE) and 1-palmitoyl-2-oleoyl-sn-glycero-3-phosphoglycerol (POPG) (Avanti Polar Lipids) were mixed at a 3:1 molar ratio, dried under argon, and vacuumed for 2 h to remove chloroform. The lipid was resuspended in 20 mM Hepes, pH 7.5, 100 mM NaCl to a final concentration of 10 mg/mL, sonicated to transparency, and incubated with 40 mM n-decyl-β-D-maltoside (DM, Anatrace) for 2 h at room temperature under gentle agitation. Wild-type or mutant human KCC1 was added at 1:100 by weight protein-to-lipid ratio. The detergent was removed by dialysis at 4 °C against the inside buffer (20 mM Hepes, pH 7.5, 100 mM Na-gluconate) in 20-kDa molecular weight cutoff dialysis cassettes. Buffer was changed every 24 h, and after 4 d of dialysis, the proteoliposomes were harvested, aliquoted, and frozen at −80 °C.

A Tl$^+$-sensitive fluorescence dye, ThaLux-AM (WaveFront Biosciences), was converted to its membrane impermeable form following a published protocol (55). After the conversion, the pH was adjusted to 7.5 with H$_2$SO$_4$. The working concentration of the dye was 50 µM. The dye was incorporated into proteoliposomes by three cycles of freeze–thaw, and then an extrusion step through a 400-nm filter (NanoSizer Extruder, T&T Scientific Corporation). Excess dye was removed through a desalting column (PD-10, GE Healthcare) equilibrated with the outside buffer (20 mM Hepes, pH 7.5, 96 mM Na-gluconate, 4 mM NaCl).

Proteoliposomes were added to a quartz cuvette, and fluorescence was monitored at 520 nm with an excitation wavelength of 494 nm (FluoroMax-4, HORIBA). The transport was initiated by addition of 0.5 mM Tl$_2$SO$_4$. When testing an inhibitor, desired concentration of the inhibitor was added to the cuvette and incubated for at least 5 min before initiation of the transport.

The rate of ion transport was estimated by the slope of a fluorescence trace in the first 30 s. Percent of activities was calculated by defining 0% for liposomes with no protein and 100% for liposomes with human KCC1 and in the absence of an inhibitor and plotted versus inhibitor concentrations. The IC$_{50}$ was obtained by fitting the data to $Y = 1/(1 + 10^{\wedge}(X-LogIC_{50}))$ using GraphPad Prism 8.0 software.

Cl$^−$ Efflux Assay in Insect Cells. The KCC-mediated Cl$^−$ efflux was measured using membrane targeted yellow fluorescent protein (mbYFPQS) as a Cl$^−$ sensitive indicator (56). Briefly, ~1.0×10^5 Sf9 insect cells were seeded per well in a poly-D-lysine–treated, black-walled, clear-bottom, 96-well plate and allowed to adhere for 45 min. Baculovirus coexpressing human KCC3 (or mutants) and mbYFPQS was generated using pFastbac-Dual (Invitrogen) and added to the Sf9 culture; baculovirus only expressing mbYFPQS was included as a negative control in all experiments. The medium was replaced 48 to 60 h postinfection by 100 µL loading buffer (20 mM Hepes, 135 mM KCl, 5 mM NaCl, 1 mM Na$_2$SO4, 1 mM MgSO$_4$, 1 mM EDTA, pH 7.4), and incubated for 2 to 3 h prior to assay. The loading buffer was exchanged to 100 µL assay buffer (20 mM Hepes, 180 mM Na-gluconate, 1 mM Na$_2$SO4, 1 mM MgSO$_4$, 1 mM EDTA, 100 µM ouabain, 10 µM bumetanide, pH 7.4) to initiate the KCC-mediated Cl$^−$ efflux;

25 µM VU0463271 was also added to half of the wells to inhibit KCC3, validating that observed Cl$^−$ efflux was mediated by KCC3. Fluorescence intensity was measured on a BioTek Synergy Neo2 HTS multi-mode microplate reader (excitation/emission wavelengths are 485 nm/535 nm). The rates of Cl$^−$ transport were calculated as the slopes of the fluorescent intensity change within the initial 60 s to 180 s for wild-type KCC1, KCC3, and ion translocation pathway mutants. For calculation of half maximal effective conventration (EC$_{50}$) for VU0463271 binding site mutants, the rates of Cl$^−$ transport were calculated using the time ranges where the slopes of the fluorescent intensity change are the steepest. An unpaired Student's t test was used to evaluate the significance of KCC-mediated, VU0463271-sensitive transport activity.

Cryo-EM Data Acquisition. The 2.5 µL of the KCC1 sample at ~6 to 8 mg/mL, with or without the VU0463271 inhibitor, was applied to glow-discharged Quantifoil 2.0/2.0 holey, 200-mesh carbon grids. Grids were plunge frozen in liquid ethane using a Vitrobot Mark III (FEI) set to 4 °C, 80% relative humidity, 20-s wait time, −1 mm offset, and 2.5-s blotting time. Data were collected on a Krios (FEI) operating at 300 kV equipped with the Gatan K3 direct electron detector at the University of Utah and Pacific Northwest Cryo-EM Center (PNCC). Images were recorded using SerialEM (57), with a defocus range between −1.0 and −3.5 µm. For the KCC1 bound with the VU0463271 sample, we recorded movies in superresolution counting mode with a physical pixel size of 1.035 Å, at a dose rate of 0.75 e$^−$/Å^2/frame, with a total exposure of 67 frames, giving a total dose of 50 e$^−$/Å^2. For the KCC1 in the 150-mM KCl sample, we also recorded movies in superresolution counting mode with a physical pixel size of 1.092 Å, at a dose rate of 1 e$^−$/Å^2/frame, with a total exposure of 40 frames, giving a total dose of 40 e$^−$/Å^2.

Image Processing, Three-Dimensional Reconstruction and Model Building. Movie frames were aligned, dose weighted, and then summed into a single micrograph using MotionCor2 (58). Contrast transfer function (CTF) parameters for micrographs were determined using the program CTFFIND4 (59). Approximately 4,000 particles were manually boxed out in cryoSPARC 3.0 to generate initial 2D averages, which were then used as template to automatically pick particles from all micrographs in cryoSPARC 3.0 (60). For the KCC1/VU0463271 dataset, a total of 2,514,195 particles were extracted and then subjected to one round of 2D classification in cryoSPARC 3.0. "Junk" particles that were sorted into incoherent or poorly resolved classes were rejected from downstream analyses. The remaining 446,018 particles from well-resolved 2D classes were pooled and subjected to another round of 2D classification in cryoSPARC 3.0, and the resulting 242,520 good particles were used to calculate a de novo model in cryoSPARC 3.0 without imposing any symmetry. At this point, the 446,018 particles from the first round of 2D classification were exported into RELION 3.0.7 (61) for multiple rounds of three-dimensional (3D) classification with C2 symmetry imposed and using the cryoSPARC 3.0 de novo map as the starting model. The 81,855 particles from one good 3D class were then subjected to nonuniform refinement in cryoSPARC 3.0 and yielded a 3.7-Å map. At this point, the 81,855 particles were again exported into RELION 3.0.7 and the orientation parameters calculated in cryoSPARC 3.0 were used for CTF refinement and Bayesian polishing (62). The polished 81,855 particles were again imported back to cryoSPARC 3.0 for nonuniform refinement

that calculated a final map of 3.49-Å resolution when the solvent noise and detergent micelle belt were masked out.

For the KCC1 in 150 mM KCl sample, a total of 4,073,077 particles were extracted and subjected to one round of 2D classification in cryoSPARC 3.0, resulting in 1,151,775 good particles. Subsequently, one round of heterogenous 3D classification was performed in cryoSPARC 3.0 without imposing any symmetry using a *Drosophila* KCC map filtered to 20-Å map as an initial model. A single class showing clear secondary structural features and best map connectivity was selected and the 306,308 particles in this class were subjected to nonuniform refinement in cryoSPARC 3.0 and yielded a 3.7-Å map. At this point, the 306,308 particles were exported into RELION 3.0.7 for 3D classification without alignment (i.e., the Euler angles and in plane shifts calculated by nonuniform refinement in cryoSPARC 3.0 were maintained) or with a local search. In both 3D classifications, the extracellular domains of KCC1 were masked out. The good 3D classes from these two 3D classification calculations were combined, and duplicated particles were removed. The resulting 79,153 particles were subjected to CTF refinement and Bayesian polishing in RELION 3.0.7 and then imported back to cryoSPARC 3.0 for nonuniform refinement that calculated a final map of 3.25-Å resolution when the solvent noise and detergent micelle belt were masked out.

The maps were locally sharpened in cryoSPARC 3.0 with an overall b factor of ~ -120 Å^2 (KCC1 in 150 mM KCl) or -150 Å^2 (KCC1 bound with UV0463271) for model building in Coot 0.8.9.3 (63). The human KCC1 transmembrane structure (PDB: 6KKR) was docked into both maps and adjusted in Coot 0.8.9.3. VU0463271 was docked into the outward-open KCC1 structure via XP scoring, standard precision docking, and Schrödinger Glide (64–66). The best pose was further refined in Phenix 1.18 (67). The cytoplasmic C-terminal domain was built de novo into the KCC1 map determined in the presence of 150 mM KCl. Most of the KCC1 C-terminal domain can be unambiguously modeled, but the region encompassing residues 882 to 929 was built tentatively due to poorly resolved densities. The model was refined in real space using PHENIX 1.18 (67), and assessed in Molprobity as shown in *SI Appendix*, Table S1 (68). Fourier Shell Correlation (FSC) curves were then calculated between the refined model versus summed half maps generated in cryoSPARC 3.0, and resolution was reported as FSC = 0.5 (*SI Appendix*, Figs. S1 and S3). University of California San Francisco Chimera was used to visualize and segment density maps, and figures were generated using Chimera and Pymol. jsPISA was used to calculate the buried surface area (69).

Molecular Dynamic Simulations. We used only the transmembrane domain (comprising residues 116 to 661) of one KCC1–VU0463271 monomer embedded in a POPC bilayer for MD simulations. We removed the VU0463271 inhibitor from the last snapshot of a 450-ns-long MD simulation to investigate the stability of the outward-open state in the absence of the inhibitor. Before starting the simulation without VU0463271, the space previously occupied by this inhibitor was filled with water molecules. The ionization state of titratable residues was determined using PropKa 3.0, assuming pH 7 (70). The simulation cells included KCC1 and its ligands, together with 359 POPC molecules, 84 Cl$^-$, 86 K$^+$ ions (in the bulk solution, corresponding to about 150-mM concentrations), and 31,224 water molecules ($\sim$150,300 atoms in total for a simulation box of $\sim$112 $\times$ 112 $\times$ 121 Å^3 size). Initial configurations of each simulation cell were assembled using Packmol-Memgen (71), part of the AmberTools software package.

MD simulations were performed with the Graphics Processing Unit (GPU) version of the Particle Mesh Ewald Molecular Dynamics (PMEMD) code (72) of the AMBER package (73). The ff14SB force field was used for the protein (74), Lipid17 for the POPC bilayer (75), TIP3P for water (76), and for the ions (77). The system was treated under periodic boundary conditions, using the particle mesh Ewald method (78) to compute long-range electrostatics. A 10-Å cutoff was used for the real part of the electrostatic and for van der Waals interactions. The SHAKE algorithm was used to constrain bonds involving hydrogen atoms (79), allowing an integration time step of 2 fs. Simulations were performed at constant temperature (310 K) and pressure (1 bar). The POPC bilayer and water solvent were allowed to equilibrate around the protein during 200 ns of MD simulations. After energy minimization, the system was gradually heated to 310 K, maintaining the protein backbone close to their positions in the cryo-EM structure by applying a harmonic restraint. Then, about 450 ns of production, MDs were performed for each model. A clustering analysis was performed based on the density of data points (80).

Author affiliations: [a]Department of Biochemistry, University of Utah School of Medicine, Salt Lake City, UT 84112; [b]Verna and Marrs McLean Department of Biochemistry and Molecular Biology, Baylor College of Medicine, Houston, TX 77030; and [c]Istituto Italiano di Tecnologia, 16163 Genova, Italy

1. G. Gamba, Molecular physiology and pathophysiology of electroneutral cation-chloride cotransporters. *Physiol. Rev.* **85**, 423–493 (2005).
2. N. Markadieu, E. Delpire, Physiology and pathophysiology of SLC12A1/2 transporters. *Pflugers Arch.* **466**, 91–105 (2014).
3. K. B. Gagnon, E. Delpire, Physiology of SLC12 transporters: Lessons from inherited human genetic mutations and genetically engineered mouse knockouts. *Am. J. Physiol. Cell Physiol.* **304**, C693–C714 (2013).
4. K. T. Kahle *et al.*, Roles of the cation-chloride cotransporters in neurological disease. *Nat. Clin. Pract. Neurol.* **4**, 490–503 (2008).
5. K. T. Kahle *et al.*, K-Cl cotransporters, cell volume homeostasis, and neurological disease. *Trends Mol. Med.* **21**, 513–523 (2015).
6. J. M. Russell, Sodium-potassium-chloride cotransport. *Physiol. Rev.* **80**, 211–276 (2000).
7. P. K. Lauf, N. C. Adragna, K-Cl cotransport: Properties and molecular mechanism. *Cell. Physiol. Biochem.* **10**, 341–354 (2000).

8. P. K. Lauf *et al.*, Erythrocyte K-Cl cotransport: Properties and regulation. *Am. J. Physiol.* **263**, C917–C932 (1992).

9. J. Glykys *et al.*, Chloride dysregulation, seizures, and cerebral edema: A relationship with therapeutic potential. *Trends Neurosci.* **40**, 276–294 (2017).

10. H. C. Howard *et al.*, The K-Cl cotransporter KCC3 is mutant in a severe peripheral neuropathy associated with agenesis of the corpus callosum. *Nat. Genet.* **32**, 384–392 (2002).

11. G. Uyanik *et al.*, Novel truncating and missense mutations of the KCC3 gene associated with Andermann syndrome. *Neurology* **66**, 1044–1048 (2006).

12. M. Puskarjov *et al.*, A variant of KCC2 from patients with febrile seizures impairs neuronal Cl- extrusion and dendritic spine formation. *EMBO Rep.* **15**, 723–729 (2014).

13. K. T. Kahle *et al.*, Genetically encoded impairment of neuronal KCC2 cotransporter function in human idiopathic generalized epilepsy. *EMBO Rep.* **15**, 766–774 (2014).

14. N. D. Merner *et al.*, Regulatory domain or CpG site variation in SLC12A5, encoding the chloride transporter KCC2, in human autism and schizophrenia. *Front. Cell. Neurosci.* **9**, 386 (2015).

15. T. Saito, A. Ishii, K. Sugai, M. Sasaki, S. Hirose, A de novo missense mutation in SLC12A5 found in a compound heterozygous patient with epilepsy of infancy with migrating focal seizures. *Clin. Genet.* **92**, 654–658 (2017).

16. T. Stödberg *et al.*, Mutations in SLC12A5 in epilepsy of infancy with migrating focal seizures. *Nat. Commun.* **6**, 8038 (2015).

17. J. Park *et al.*, *De novo* variants in *SLC12A6* cause sporadic early-onset progressive sensorimotor neuropathy. *J. Med. Genet.* **57**, 283–288 (2020).

18. W. Löscher, M. Puskarjov, K. Kaila, Cation-chloride cotransporters NKCC1 and KCC2 as potential targets for novel antiepileptic and antiepileptogenic treatments. *Neuropharmacology* **69**, 62–74 (2013).

19. E. Delpire, K. T. Kahle, The KCC3 cotransporter as a therapeutic target for peripheral neuropathy. *Expert Opin. Ther. Targets* **21**, 113–116 (2017).

20. P. Q. Duy, W. B. David, K. T. Kahle, Identification of KCC2 mutations in human epilepsy suggests strategies for therapeutic transporter modulation. *Front. Cell. Neurosci.* **13**, 515 (2019).

21. B. Chen *et al.*, Reactivation of dormant relay pathways in injured spinal cord by KCC2 manipulations. *Cell* **174**, 1599 (2018).

22. M. Gagnon *et al.*, Chloride extrusion enhancers as novel therapeutics for neurological diseases. *Nat. Med.* **19**, 1524–1528 (2013).

23. F. C. Brown *et al.*, Activation of the erythroid K-Cl cotransporter Kcc1 enhances sickle cell disease pathology in a humanized mouse model. *Blood* **126**, 2863–2870 (2015).

24. B. E. Shmukler *et al.*, Genetic disruption of KCC cotransporters in a mouse model of thalassemia intermedia. *Blood Cells Mol. Dis.* **81**, 102389 (2020).

25. L. Malha, S. J. Mann, Loop diuretics in the treatment of hypertension. *Curr. Hypertens. Rep.* **18**, 27 (2016).

26. A. D. Sinha, R. Agarwal, Thiazide diuretics in chronic kidney disease. *Curr. Hypertens. Rep.* **17**, 13 (2015).

27. A. Ward, R. C. Heel, Bumetanide. A review of its pharmacodynamic and pharmacokinetic properties and therapeutic use. *Drugs* **28**, 426–464 (1984).

28. L. P. Rybak, Ototoxicity of loop diuretics. *Otolaryngol. Clin. North Am.* **26**, 829–844 (1993).

29. G. Chi *et al.*, Phospho-regulation, nucleotide binding and ion access control in potassium-chloride cotransporters. *EMBO J.* **40**, e107294 (2021).

30. T. A. Chew *et al.*, Structure and mechanism of the cation-chloride cotransporter NKCC1. *Nature* **572**, 488–492 10.1038/s41586-019-1438-2. (2019).

31. X. Yang, Q. Wang, E. Cao, Structure of the human cation-chloride cotransporter NKCC1 determined by single-particle electron cryo-microscopy. *Nat. Commun.* **11**, 1016 (2020).

32. S. Liu *et al.*, Cryo-EM structures of the human cation-chloride cotransporter KCC1. *Science* **366**, 505–508 (2019).

33. M. S. Reid, D. M. Kern, S. G. Brohawn, Cryo-EM structure of the potassium-chloride cotransporter KCC4 in lipid nanodiscs. *eLife* **9**, e52505 (2020).

34. S. Zhang *et al.*, The structural basis of function and regulation of neuronal cotransporters NKCC1 and KCC2. *Commun. Biol.* **4**, 226 (2021).

35. Y. Xie *et al.*, Structures and an activation mechanism of human potassium-chloride cotransporters. *Sci. Adv.* **6**, eabc5883 (2020).

36. X. Chi *et al.*, Cryo-EM structures of the full-length human KCC2 and KCC3 cation-chloride cotransporters. *Cell Res.* **31**, 482–484 (2021).

37. Y. Shi, Common folds and transport mechanisms of secondary active transporters. *Annu. Rev. Biophys.* **42**, 51–72 (2013).

38. D. Drew, O. Boudker, Shared molecular mechanisms of membrane transporters. *Annu. Rev. Biochem.* **85**, 543–572 (2016).

39. E. Delpire *et al.*, Further optimization of the K-Cl cotransporter KCC2 antagonist ML077: Development of a highly selective and more potent in vitro probe. *Bioorg. Med. Chem. Lett.* **22**, 4532–4535 (2012).

40. E. Delpire *et al.*, Small-molecule screen identifies inhibitors of the neuronal K-Cl cotransporter KCC2. *Proc. Natl. Acad. Sci. U.S.A.* **106**, 5383–5388 (2009).

41. M. Y. Monette, S. Somasekharan, B. Forbush, Molecular motions involved in Na-K-Cl cotransporter-mediated ion transport and transporter activation revealed by internal cross-linking between transmembrane domains 10 and 11/12. *J. Biol. Chem.* **289**, 7569–7579 (2014).

42. S. Somasekharan, J. Tanis, B. Forbush, Loop diuretic and ion-binding residues revealed by scanning mutagenesis of transmembrane helix 3 (TM3) of Na-K-Cl cotransporter (NKCC1). *J. Biol. Chem.* **287**, 17308–17317 (2012).

43. I. Giménez, B. Forbush, The residues determining differences in ion affinities among the alternative splice variants F, A, and B of the mammalian renal Na-K-Cl cotransporter (NKCC2). *J. Biol. Chem.* **282**, 6540–6547 (2007).

44. M. Y. Monette, J. Rinehart, R. P. Lifton, B. Forbush, Rare mutations in the human Na-K-Cl cotransporter (NKCC2) associated with lower blood pressure exhibit impaired processing and transport function. *Am. J. Physiol. Renal Physiol.* **300**, F840–F847 (2011).

45. H. Krishnamurthy, E. Gouaux, X-ray structures of LeuT in substrate-free outward-open and apo inward-open states. *Nature* **481**, 469–474 (2012).

46. J. A. Coleman *et al.*, Serotonin transporter-ibogaine complexes illuminate mechanisms of inhibition and transport. *Nature* **569**, 141–145 (2019).

47. A. Penmatsa, E. Gouaux, How LeuT shapes our understanding of the mechanisms of sodium-coupled neurotransmitter transporters. *J. Physiol.* **592**, 863–869 (2014).

48. A. Watanabe *et al.*, The mechanism of sodium and substrate release from the binding pocket of vSGLT. *Nature* **468**, 988–991 (2010).

49. J. Rinehart *et al.*, Sites of regulated phosphorylation that control K-Cl cotransporter activity. *Cell* **138**, 525–536 (2009).

50. K. Inoue, J. Yamada, S. Ueno, A. Fukuda, Brain-type creatine kinase activates neuron-specific K+/Cl- co-transporter KCC2. *J. Neurochem.* **96**, 598–608 (2006).

51. A. Salin-Cantegrel *et al.*, HMSN/ACC truncation mutations disrupt brain-type creatine kinase-dependant activation of K+/Cl- co-transporter 3. *Hum. Mol. Genet.* **17**, 2703–2711 (2008).

52. S. K. Singh, C. L. Piscitelli, A. Yamashita, E. Gouaux, A competitive inhibitor traps LeuT in an open-to-out conformation. *Science* **322**, 1655–1661 (2008).

53. J. A. Coleman, E. M. Green, E. Gouaux, X-ray structures and mechanism of the human serotonin transporter. *Nature* **532**, 334–339 (2016).

54. A. Goehring *et al.*, Screening and large-scale expression of membrane proteins in mammalian cells for structural studies. *Nat. Protoc.* **9**, 2574–2585 (2014).

55. B. F. Dutter, A. Ender, G. A. Sulikowski, C. D. Weaver, Rhodol-based thallium sensors for cellular imaging of potassium channel activity. *Org. Biomol. Chem.* **16**, 5575–5579 (2018).

56. S. D. Watts, K. L. Suchland, S. G. Amara, S. L. Ingram, A sensitive membrane-targeted biosensor for monitoring changes in intracellular chloride in neuronal processes. *PLoS One* **7**, e35373 (2012).

57. D. N. Mastronarde, Automated electron microscope tomography using robust prediction of specimen movements. *J. Struct. Biol.* **152**, 36–51 (2005).

58. S. Q. Zheng *et al.*, MotionCor2: Anisotropic correction of beam-induced motion for improved cryo-electron microscopy. *Nat. Methods* **14**, 331–332 (2017).

59. A. Rohou, N. Grigorieff, CTFFIND4: Fast and accurate defocus estimation from electron micrographs. *J. Struct. Biol.* **192**, 216–221 (2015).

60. A. Punjani, J. L. Rubinstein, D. J. Fleet, M. A. Brubaker, cryoSPARC: Algorithms for rapid unsupervised cryo-EM structure determination. *Nat. Methods* **14**, 290–296 (2017).

61. S. H. Scheres, RELION: Implementation of a Bayesian approach to cryo-EM structure determination. *J. Struct. Biol.* **180**, 519–530 (2012).

62. J. Zivanov, T. Nakane, S. H. W. Scheres, A Bayesian approach to beam-induced motion correction in cryo-EM single-particle analysis. *IUCrJ* **6**, 5–17 (2019).

63. P. Emsley, B. Lohkamp, W. G. Scott, K. Cowtan, Features and development of Coot. *Acta Crystallogr. D Biol. Crystallogr.* **66**, 486–501 (2010).

64. Anonymous, *Schrödinger Release 2021-4: Glide* (Schrödinger, LLC, New York, NY, 2021).

65. R. A. Friesner *et al.*, Glide: A new approach for rapid, accurate docking and scoring. 1. Method and assessment of docking accuracy. *J. Med. Chem.* **47**, 1739–1749 (2004).

66. R. A. Friesner *et al.*, Extra precision glide: Docking and scoring incorporating a model of hydrophobic enclosure for protein-ligand complexes. *J. Med. Chem.* **49**, 6177–6196 (2006).

67. P. D. Adams *et al.*, PHENIX: A comprehensive Python-based system for macromolecular structure solution. *Acta Crystallogr. D Biol. Crystallogr.* **66**, 213–221 (2010).

68. C. J. Williams *et al.*, MolProbity: More and better reference data for improved all-atom structure validation. *Protein Sci.* **27**, 293–315 (2018).

69. E. Krissinel, Stock-based detection of protein oligomeric states in jsPISA. *Nucleic Acids Res.* **43** (W1), W314-9 (2015).

70. M. H. Olsson, C. R. Søndergaard, M. Rostkowski, J. H. Jensen, PROPKA3: Consistent treatment of internal and surface residues in empirical pKa predictions. *J. Chem. Theory Comput.* **7**, 525–537 (2011).

71. S. Schott-Verdugo, H. Gohlke, PACKMOL-Memgen: A simple-to-use, generalized workflow for membrane-protein-lipid-bilayer system building. *J. Chem. Inf. Model.* **59**, 2522–2528 (2019).

72. S. Le Grand, A. W. Gotz, R. C. Walker, SPFP: Speed without compromise-A mixed precision model for GPU accelerated molecular dynamics simulations. *Comput. Phys. Commun.* **184**, 374–380 (2013).

73. R. Salomon-Ferrer, D. A. Case, R. C. Walker, An overview of the Amber biomolecular simulation package. *Wires Comput Mol Sci* **3**, 198–210 (2013).

74. J. A. Maier *et al.*, ff14SB: Improving the accuracy of protein side chain and backbone parameters from ff99SB. *J. Chem. Theory Comput.* **11**, 3696–3713 (2015).

75. C. J. Dickson *et al.*, Lipid14: The Amber lipid force field. *J. Chem. Theory Comput.* **10**, 865–879 (2014).

76. W. L. Jorgensen, J. Chandrasekhar, J. D. Madura, R. W. Impey, M. L. Klein, Comparison of simple potential functions for simulating liquid water. *J. Chem. Phys.* **79**, 926–935 (1983).

77. I. S. Joung, T. E. Cheatham III, Determination of alkali and halide monovalent ion parameters for use in explicitly solvated biomolecular simulations. *J. Phys. Chem. B* **112**, 9020–9041 (2008).

78. T. Darden, D. York, L. Pedersen, Particle mesh Ewald - an N.Log(N) method for Ewald sums in large systems. *J. Chem. Phys.* **98**, 10089–10092 (1993).

79. J. P. Ryckaert, G. Ciccotti, H. J. C. Berendsen, Numerical-integration of Cartesian equations of motion of a system with constraints - Molecular-dynamics of N-alkanes. *J. Comput. Phys.* **23**, 327–341 (1977).

80. A. Rodriguez, A. Laio, Machine learning. Clustering by fast search and find of density peaks. *Science* **344**, 1492–1496 (2014).

81. Y. X. Zhao, E. H. Cao, Human KCC1 bound with YU0463271 in an outward-open state. Electron Microscopy Data Bank. https://deposit-1.wwpdb.org/deposition/pageview/depsummary. Deposited 2 February 2022.

82. Y. X. Zhao, E. H. Cao, Human potassium-chloride cotransporter 1 in inward-open state. Electron Microscopy Data Bank. https://deposit-1.wwpdb.org/deposition/pageview/depsummary. Deposited 2 February 2022.

83. Y. X. Zhao, E. H. Cao, Human KCC1 bound with VU0463271 in an outward-open state. Protein Data Bank. https://deposit-1.wwpdb.org/deposition/pageview/depsummary. Deposited 2 February 2022.

84. Y. X. Zhao, E. H. Cao, Human potassium-chloride cotransporter 1 in inward-open state. Protein Data Bank. https://deposit-1.wwpdb.org/deposition/pageview/depsummary. Deposited 2 February 2022.